

Emergent transverse-field Ising model in d^4 spin-orbit Mott insulators

Jiří Chaloupka

Department of Condensed Matter Physics, Faculty of Science,
Masaryk University, Kotlářská 2, 61137 Brno, Czech Republic

(Dated: January 8, 2024)

Mott-insulating transition metal oxides containing t_{2g}^4 ions with strong spin-orbit coupling were recently demonstrated to display unusual magnetism due to a dynamical mixing of the low-energy multiplet states via exchange processes. Here we derive exchange interactions in the situation where a tetragonal or trigonal crystal field selects a single relevant excited state on top of the singlet ionic ground state, producing an effective spin- $\frac{1}{2}$. We show that these moments universally obey antiferromagnetic transverse-field Ising model (TFIM) with an intrinsic transverse field generated by the splitting of the two ionic singlets. Using Ru^{4+} as an example ion, we provide quantitative estimates of the exchange and illustrate the emergent TFIM physics based on phase diagrams and excitation spectra obtained for several 2D lattices – square, honeycomb, as well as for the frustrated triangular lattice.

Introduction. Transverse-field Ising model introduced by de Gennes in 1960s [1] ranks among the most prominent example systems to study quantum criticality [2, 3]. Its Ising part belongs to a few lattice models in statistical physics for which exact solutions are available [4–9] and gained popularity as a prototype model to capture collective behavior not only of localized spins in magnets but also in a much broader context [10, 11]. Ising model itself represents a classical problem. By adding transverse magnetic field, the quantum nature of spins comes into play, leading to a quantum critical behavior reflecting a competition of Ising interactions and Zeeman energy. The model has been studied in various settings, a particularly appealing case is the antiferromagnetic (AF) TFIM on a triangular lattice combining quantum criticality with frustration and exhibiting Berezinskii-Kosterlitz-Thouless (BKT) transitions [12–14].

Realization of TFIM in magnetic materials is limited by the requirement of strong uniaxial anisotropy of exchange interactions and their suitable strength with respect to accessible magnetic fields. Simple anisotropic ferromagnets were considered since the early days [15], however a definitive experimental demonstration came only in 2010 with CoNb_2O_6 acting as 1D TFIM chain in neutron scattering [16]. The case of frustrated AF TFIM is yet more delicate. A promising route was recently suggested by $4f$ triangular-lattice compound TmMgGaO_4 where signatures of BKT physics were observed [17–19]. Here the lowest two levels of Tm^{3+} ions form a well-isolated pair of singlets hosting effective spin- $\frac{1}{2}$. Thanks to large spin-orbit coupling (SOC) and hence large orbital component of these moments, they are subject to strongly anisotropic interactions. The second key ingredient is the crystal-field (CF) induced splitting of the two singlets that plays a role of an *intrinsic* transverse field [20–23]. In this Letter we show that $4d^4$ and $5d^4$ Mott insulators with large SOC [24] may be even more convenient platform for TFIM utilizing a similar mechanism. As we demonstrate by explicitly deriving the exchange model, at sufficiently large negative CF splitting of t_{2g} levels, the interactions are of AF Ising-type en-

forced by the very structure of the d^4 ionic states. This promises a realization of TFIM on various 2D lattices at larger energy scales and corresponding characteristic temperatures as compared to $4f$ systems (exchange strength reaching tens of meV compared to ≈ 1 meV for TmMgGaO_4 [17]), with the intrinsic transverse field potentially tunable by straining.

TFIM imposed by spin-orbital structure of ionic states. We first briefly review the multiplet structure of relevant ions such as Ru^{4+} or Ir^{5+} with d^4 valence configuration limited to t_{2g} orbitals. Large SOC in these ions forms non-magnetic $J = 0$ singlet ground state s and low-energy $J = 1$ triplet excitations T_x, T_y, T_z separated from the ground-state level by energy $\zeta/2$ with ζ denoting the single-electron SOC strength [24]. These states may serve as a basis for an effective model exhibiting quantum critical behavior due to the competition of exchange and triplet energy cost [24, 25]. The essential control parameter here is the tetragonal or trigonal CF splitting Δ of t_{2g} orbital levels relevant for 2D lattices of corner-sharing or edge-sharing metal- O_6 octahedra, respectively. Nonzero Δ splits the $J = 1$ triplet and strongly modifies the ionic excitation energies as plotted in Fig. 1(a) and thoroughly discussed in [26]. Earlier works analyzed the situation with no triplet splitting [25, 27, 28] and partially the positive- Δ case [29, 30]. Here we focus on the so far unexplored negative- Δ case with $|\Delta| \gtrsim \zeta$, the relevant set of basis states thus gets reduced to a non-Kramers doublet consisting of the ionic ground state s and one of the triplets T_z selected by the out-of-plane CF axis direction z [see Fig. 1(a),(e)]. The internal structure of these t_{2g}^4 states sketched in Fig. 1(b) is best appreciated when expressing them via eigenstates $|L_z, S_z\rangle$ of the total effective t_{2g} orbital momentum $L = 1$ and total spin $S = 1$ carried by the two t_{2g} holes:

$$\begin{aligned} |s\rangle &= \frac{1}{\sqrt{2}}(|+1, -1\rangle + |-1, +1\rangle) \cos \vartheta_0 - |0, 0\rangle \sin \vartheta_0, \\ |T_z\rangle &= \frac{i}{\sqrt{2}}(|+1, -1\rangle - |-1, +1\rangle). \end{aligned} \quad (1)$$

The auxiliary angle ϑ_0 is given by $\tan 2\vartheta_0 = 2\sqrt{2}/(1 - 2\delta)$ with $\delta = \Delta/\zeta$ and vanishes in $\Delta \rightarrow -\infty$ limit [see

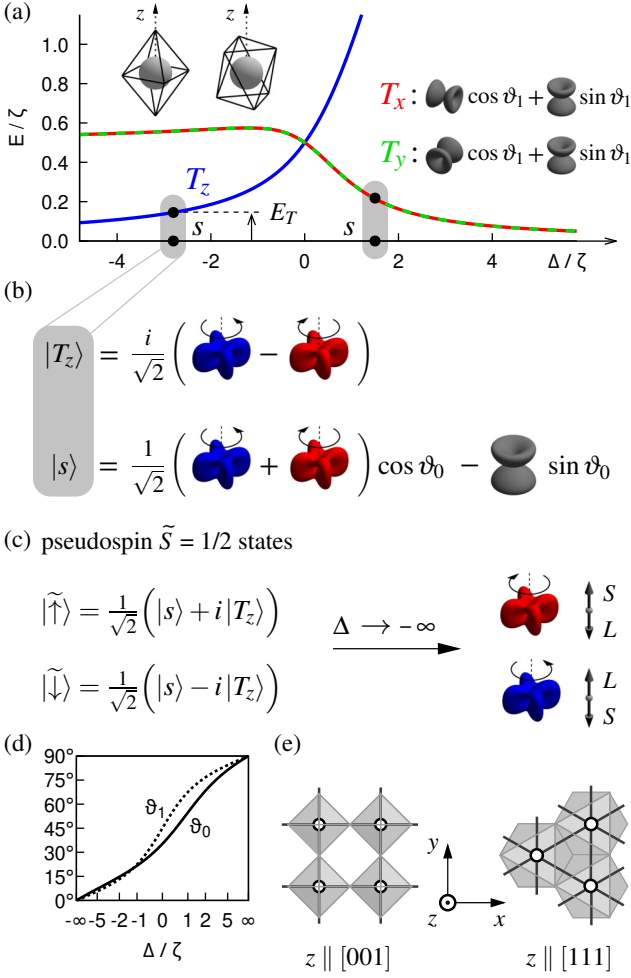


FIG. 1. (a) Low-energy levels of t_{2g}^4 ion depending on tetragonal or trigonal CF splitting Δ . The energies are plotted relative to the ionic ground-state level. Within LS coupling scheme, total $L = 1$ and $S = 1$ of the two holes added to the t_{2g}^6 configuration are combined by SOC into ground-state singlet s , a triplet of states $T_{x,y,z}$ degenerate at $\Delta = 0$, and a quintuplet at higher energies that may be ignored. In point-charge model, negative Δ corresponds to the indicated tetragonal/trigonal elongation of metal- O_6 octahedra (in reality it is influenced also by the Madelung potential contributed by more distant ions and covalency effects which may break this simple correspondence). (b) At large enough $\Delta < 0$, the pair s and T_z forms the basis of the low-energy model. The corresponding wave functions (for the tetragonal case) are represented by shapes of the respective hole densities resolved according to S_z and L_z . Spin is indicated by color (red: up along z , blue: down), orbital angular momentum by an arrow. The remaining $T_{x,y}$ are shown in the inset of (a). (c) Linear combinations of s and T_z forming the basis of the pseudospin $\tilde{S} = \frac{1}{2}$ model. For large negative Δ they converge to fully polarized states with antiparallel L and S . (d) Δ -dependent angles $\vartheta_{0,1}$ entering the wave functions. (e) xyz reference frame with z being the out-of-plane axis.

Fig. 1(d)]. The splitting of s and T_z levels equals $E_T = \frac{1}{4}\zeta[\sqrt{(1-2\delta)^2+8} - (1-2\delta)]$, vanishing as $\zeta/(1-2\delta)$.

The exchange interactions between d^4 ions in the above regime can be obtained by standard second-order perturbation theory in electron hopping resulting in a model for hardcore bosons s and T_z . These are subject to the local constraint $n_s + n_{T_z} = 1$, where $n_s = s^\dagger s$ and $n_{T_z} = T_z^\dagger T_z$ count bosons on a given site. The model becomes particularly transparent if formulated in terms of a pseudospin $\tilde{S} = \frac{1}{2}$ based on the linear combinations $|\tilde{\uparrow}\rangle, |\tilde{\downarrow}\rangle = \frac{1}{\sqrt{2}}(|s\rangle \pm i|T_z\rangle)$:

$$\begin{aligned} |\tilde{\uparrow}\rangle &= c^2|-1, +1\rangle - s^2|+1, -1\rangle - \sqrt{2}cs|0, 0\rangle, \\ |\tilde{\downarrow}\rangle &= c^2|+1, -1\rangle - s^2|-1, +1\rangle - \sqrt{2}cs|0, 0\rangle \end{aligned} \quad (2)$$

with $c = \cos \frac{\vartheta_0}{2}$ and $s = \sin \frac{\vartheta_0}{2}$. This choice is motivated by the $\Delta \rightarrow -\infty$ limit depicted in Fig. 1(c) where $|\tilde{\uparrow}\rangle, |\tilde{\downarrow}\rangle$ correspond to fully polarized states $|-1, +1\rangle, |+1, -1\rangle$ with strictly antiparallel out-of-plane $L_z = -S_z$. Moreover, the pseudospin carries Van Vleck-type magnetic moment which is purely out-of-plane with large $g_z = 6 \cos \vartheta_0$ and zero g_{xy} [26]. On the operator level, this change of the basis is expressed via the correspondence relations $\tilde{S}_x = \frac{1}{2} - n_{T_z}$, $\tilde{S}_y = \frac{1}{2}(s^\dagger T_z + T_z^\dagger s)$, $\tilde{S}_z = -\frac{i}{2}(s^\dagger T_z - T_z^\dagger s)$. As a consequence, the level splitting E_T translates to a transverse field $h = E_T$ in the pseudospin formulation. The form of the exchange interactions can be easily anticipated by considering the $\Delta \rightarrow -\infty$ limit in Fig. 1(c). Since the two virtual electronic hoppings generating second-order exchange can only change the ionic spin component S_z by $\Delta S_z = 0, \pm 1$, the states $|\tilde{\uparrow}\rangle, |\tilde{\downarrow}\rangle$ with $S_z = \pm 1$ cannot be connected and the exchange is strictly of Ising $\tilde{S}_z \tilde{S}_z$ type in this limit. A full derivation for general $\Delta \lesssim -\zeta$ gives the pseudospin model

$$\mathcal{H}_{\tilde{S}} = \sum_{\langle ij \rangle} \left(J_z \tilde{S}_i^z \tilde{S}_j^z + J_x \tilde{S}_i^x \tilde{S}_j^x + J_y \tilde{S}_i^y \tilde{S}_j^y \right) - (h + \delta h) \sum_i \tilde{S}_i^x \quad (3)$$

with dominant J_z and $h = E_T$, supplemented by minor $J_x, J_y, \delta h$. In contrast to J_z , the latter exchange parameters only arise due to the small common parts of $|\tilde{\uparrow}\rangle, |\tilde{\downarrow}\rangle$ and as such they are proportional to $\sin^2 \vartheta_0$. As demonstrated later, they quickly drop when entering the $\Delta \lesssim -\zeta$ regime. Detailed exchange expressions for both 180° bonds (corner-sharing metal- O_6 octahedra) and 90° bonds (edge-sharing) as well as the connection to the hardcore boson formulations are given in [26]. Note that due to the omission of the bond-directional states $T_{x,y}$, the interactions are identical for all bond directions. Neglecting the minor contributions in Eq. (3), we arrive at the final minimal model which takes the form of transverse-field Ising model

$$\mathcal{H}_{\text{TFIM}} = J_z \sum_{\langle ij \rangle} \tilde{S}_i^z \tilde{S}_j^z - h \sum_i \tilde{S}_i^x. \quad (4)$$

Let us emphasize that this minimal model is imposed solely by the internal structure of the ionic states at sufficiently negative Δ/ζ , hence the mechanism is universal for any lattice.

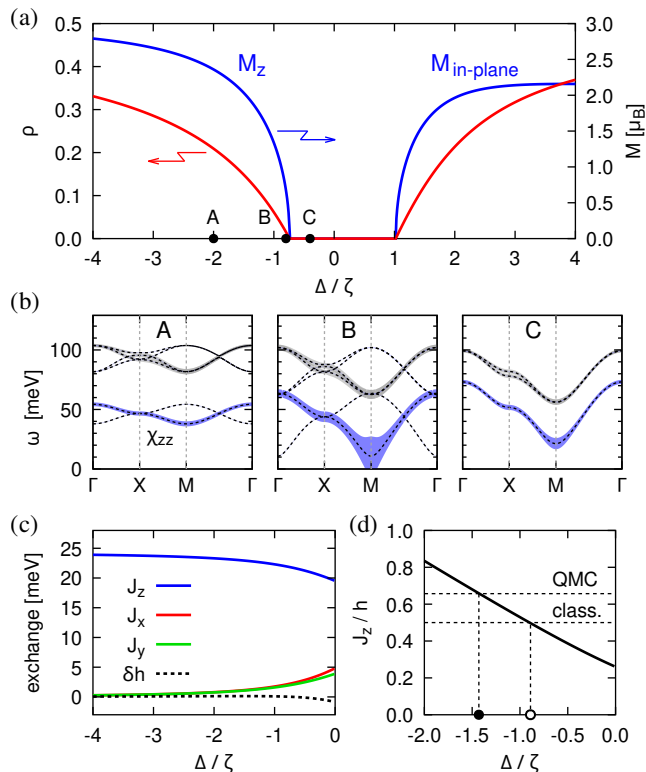


FIG. 2. (a) Variational phase diagram of the full s - \mathbf{T} model for the square lattice obtained using $U = 3$ eV, $J_H = 0.5$ eV, $\zeta = 0.15$ eV (roughly corresponding to Ru^{4+}), and hopping $t = 0.14$ eV. At large enough negative/positive Δ , condensate of \mathbf{T} -bosons with the density ρ is present and carries out-of-plane/in-plane AF moment. (b) Dynamic magnetic susceptibility calculated by LFWT at selected points in (a) and separated into zz component (blue) and in-plane $xx + yy$ part (gray). Line thickness scales with the intensity, dashed lines indicate the dispersions of excitations. Triangular Brillouin-zone path including high-symmetry points $\Gamma = (0,0)$, $X = (\pi,0)$, and $M = (\pi,\pi)$ is used. Identical zz component spectra are obtained also by LFWT limited to s and T_z bosons only. (c) Plot of the interaction parameters of the effective pseudospin- $\frac{1}{2}$ model (3) showing the clear dominance of J_z . (d) Parameter ratio J_z/h of the effective model plotted as function of Δ/ζ . The QCP position on Δ/ζ axis is estimated by mapping the critical ratio $(J_z/h)_{\text{crit}}$ of TFIM determined either classically (0.5) or using precise QMC result (≈ 0.657) back to Δ/ζ .

Exchange parameters, phase diagrams, and excitations. In this section, we illustrate the emergence of TFIM as a low-energy magnetic model by exploring phases and excitations obtained using an exchange model including all four low-energy states $s, T_{x,y,z}$ in the local basis. This model, to be called (full) s - \mathbf{T} model in the following, has the advantage to be applicable at any Δ/ζ and allows us to study the crossover to the $\Delta \lesssim -\zeta$ regime of interest. As we show below, the main features in this regime can indeed be understood and reproduced by simple AF TFIM. Its connection to the full s - \mathbf{T} model is provided by projection onto s and T_z , which

transforms the s - \mathbf{T} model into the pseudospin- $\frac{1}{2}$ model of Eq. (3). On the way, we will also give quantitative hints on the TFIM parameters targeting Ru^{4+} compounds by the particular choice of Hubbard repulsion U , Hund's coupling J_H , and SOC strength ζ . The s - \mathbf{T} model Hamiltonian was obtained by second-order perturbation theory and encompasses a large number of bond terms involving hardcore bosons $s, T_{x,y,z}$, following the general structure presented in [26]. Due to this complexity, it cannot be given explicitly here (see [25] for a simpler version with $\Delta/\zeta = J_H/U = 0$), but we use it in full to determine the variational phase diagram using the trial product state

$$|\Psi_{\text{trial}}\rangle = \prod_{i \in \text{sites}} \left(\sqrt{1 - \rho_i} s^\dagger + \sqrt{\rho_i} \sum_{\alpha=x,y,z} d_{i\alpha}^* T_{i\alpha}^\dagger \right) |\text{vac}\rangle \quad (5)$$

and to calculate corresponding harmonic excitations using linear flavor wave theory (LFWT) [26, 31–35]. $|\Psi_{\text{trial}}\rangle$ of Eq. (5) enables to capture various forms of magnetically ordered states linked to a condensation of hardcore vector bosons \mathbf{T} as well as the paramagnetic state where \mathbf{T} remain uncondensed. In the former case, the site-dependent variational parameters ρ_i (scalars) and \mathbf{d}_i (unit vectors) determine the condensate density and magnetic structure, respectively. The associated excitation spectrum contains magnon-like modes (fluctuations in \mathbf{d}) and amplitude mode (oscillations of the condensate density ρ). In the latter paramagnetic case, we find a trivial minimum with all $\rho_i = 0$ and excitations being carried directly by bosons \mathbf{T} .

As a first example, Fig. 2 gives an overview for a square lattice with straight 180° bonds, where the nearest-neighbor hopping t connects diagonally a pair of t_{2g} orbitals active on a given bond [24]. The phase diagram shown in Fig. 2(a) contains a window of paramagnetic (PM) phase around $\Delta/\zeta = 0$, separated by quantum critical points (QCP) at $\Delta \approx \pm\zeta$ from two condensed phases. Both are characterized by AF ordered Van Vleck moments but their nature strongly differs. The positive- Δ case with in-plane moments can be described by a pseudospin-1 model with predominantly XY-type of interactions and has been discussed in the context of Ca_2RuO_4 [26, 29, 30] which was estimated to have $\Delta/\zeta \approx 1.5$ [29]. In contrast, our negative- Δ case of interest is captured by the above pseudospin- $\frac{1}{2}$ TFIM. In this language, the pseudospins in the PM phase are fully aligned by the in-plane transverse field $h = E_T$, while beyond QCP they develop staggered out-of-plane component supported by $J_z > 0$. Due to zero in-plane g -factor, only the AF out-of-plane component carries magnetic moment.

The TFIM picture is confirmed by the excitation spectra in Fig. 2(b). Near the QCP, the dispersion of the low-energy excitations probed by χ_{zz} softens at the AF momentum $M = (\pi,\pi)$, deeper in the AF phase they become flat and the gap saturates, which is consistent with the expected Ising-type excitation at constant $\omega = 2J_z$ contrasting to the magnon-like excitations for positive Δ [26]. The proximity to TFIM is illus-

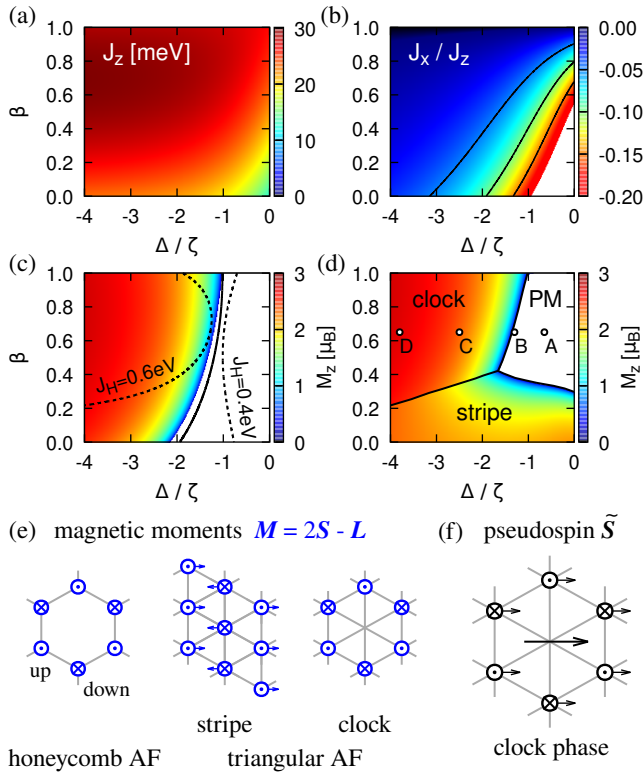


FIG. 3. (a) Effective exchange parameter J_z for the 90° bonding geometry and $U = 3$ eV, $J_H = 0.5$ eV, $\zeta = 0.15$ eV. The parameter β interpolates linearly between metal-O-metal hopping t and direct hopping t' , namely $t = (1 - \beta) \times 0.3$ eV, $t' = \beta \times 0.3$ eV. (b) Relative strength of J_x ($\approx J_y$) compared to the dominant J_z . (c) Variational phase diagram of the full s - \mathbf{T} model on the honeycomb lattice. Major part is taken by AF phase with out-of-plane moments, the white area corresponds to the PM phase. The (classical) phase boundary of the resulting TFIM (i.e. pseudospin- $\frac{1}{2}$ model with $J_{x,y}$ neglected) is shown by the solid line. Dashed lines illustrate its trend for varying J_H . (d) Variational phase diagram for the triangular lattice. Using the critical ratios for TFIM from QMC [36] together with our TFIM parameters, the estimated phase boundary gets shifted horizontally by about 0.3 to the left in (c) and by 1.2 in (d). (e) Magnetic patterns of the phases in (c),(d). (f) Clock-phase pattern in the pseudospin- $\frac{1}{2}$ representation. The central site carries a saturated in-plane moment which is completely hidden in the magnetic pattern due to the zero in-plane g -factor.

trated by the evaluated parameters of the pseudospin- $\frac{1}{2}$ model (3) presented in Fig. 2(c). For $\Delta \lesssim -\zeta$, the dominant AF J_z quickly saturates at the infinite- Δ value $J_z \approx (5 - 7\eta) t^2 / U$ with $\eta = J_H / U$ [26], and is accompanied by tiny in-plane $J_{x,y}$. Finally, Fig. 2(d) combines J_z of Fig. 2(c) and $h = E_T$ found in Fig. 1(a) into the ratio J_z/h that is the decisive parameter of TFIM and can be used to estimate the critical value of Δ/ζ . The value $(\Delta/\zeta)_{\text{crit}} \approx -0.9$ based on $(J_z/h)_{\text{crit}} = 0.5$ obtained by treating TFIM classically roughly agrees with our variational result for the full s - \mathbf{T} model in Fig. 2(a). It gets corrected towards more negative $(\Delta/\zeta)_{\text{crit}} \approx -1.4$ when

using the precise value $(J_z/h)_{\text{crit}} \approx 0.657$ obtained by QMC [37].

Similar analysis is performed for 90° bond geometry that occurs in e.g. honeycomb or triangular lattices with edge-sharing octahedra. Here two major hopping channels active on metal₂-O₂ plaquettes have to be simultaneously considered – bonding paths via oxygen ions and a direct overlap of d orbitals [24]. The former hopping with amplitude t connects off-diagonally a bond-dependent pair of t_{2g} orbitals while the complementary t_{2g} orbital is subject to direct hopping t' . Despite the completely different hopping rules as compared to the 180° case, the pseudospin- $\frac{1}{2}$ interactions plotted in Figs. 3(a),(b) again feature dominant AF Ising J_z accompanied by minor in-plane $J_{x,y}$, in accord with the general conclusions of the previous section. For large negative Δ , the value of J_z approaches $J_z \approx \frac{4}{9} [(7 - 20\eta) t^2 + (2 + 8\eta) t t' + (4 - 8\eta) t'^2] / U$.

Variational phase diagram for the non-frustrated honeycomb lattice presented in Fig. 3(c) and the corresponding excitation spectrum [26] show similar behavior as for the square lattice. Much richer is the case of the frustrated triangular lattice. The phase diagram shown in Fig. 3(d) contains two condensed phases with non-trivial patterns depicted in Fig. 3(e),(f). One of them appears in so-called clock phase familiar from the studies of TFIM on triangular lattice [13, 14]. Here the frustration of pseudospins is resolved by a formation of honeycomb AF pattern of the out-of-plane components to satisfy the Ising interactions and a simultaneous alignment of the in-plane components with the transverse field. At the remaining sites, the pseudospins are strictly in-plane, avoiding the Ising interactions and conforming fully to the transverse field. The other pattern – of stripy type – is specific to our s - \mathbf{T} model and is not captured by the pseudospin- $\frac{1}{2}$ TFIM because of the participation of $T_{x,y}$ in the condensate. Based on the extended nature of $4d$ and $5d$ orbitals, the regime $t' \gtrsim t$ can be expected, making the clock phase more relevant.

Interestingly, the clock pattern of pseudospins on triangular lattice is obscured by zero in-plane g -factor, giving rise to a static magnetic pattern identical to that of the honeycomb AF phase. However, the excitation spectra reveal a fundamental difference to the latter case. Figure 4(a) shows the evolution of the magnetic excitations when crossing the PM/clock phase boundary. These are again obtained using the full s - \mathbf{T} model, but – as demonstrated by Fig. 4(b) – the relevant χ_{zz} is perfectly reproduced also by the pseudospin dynamics within the corresponding TFIM. Approaching the PM/clock boundary, the excitations soften at the characteristic momentum $K = 2\pi(\frac{1}{\sqrt{3}}, \frac{1}{3})$ of the honeycomb AF pattern formed after entering the clock phase. Here a separation of energy scales occurs. The high-energy part of the spectrum is represented by a flat Ising-type excitation at $\omega \approx 2J_z$ encountered previously and linked here to a pseudospin flip taking place in the honeycomb AF structure. This excitation is complemented by a dispersing low-energy mode (energy scale h) that involves rotations

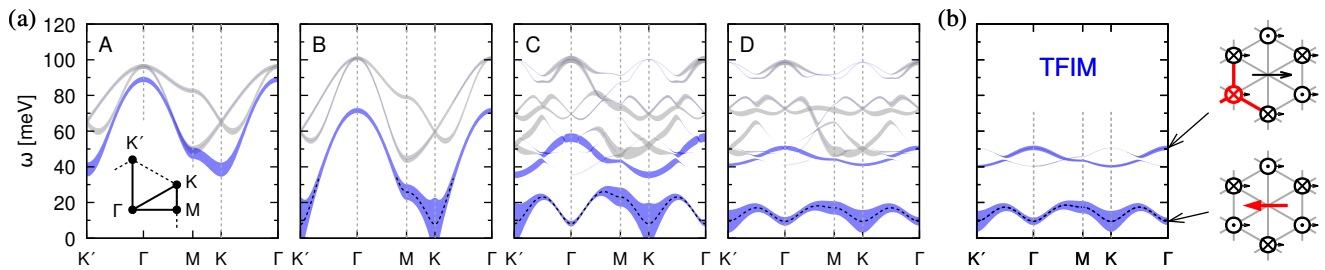


FIG. 4. (a) Magnetic excitation spectra for the selected points indicated in Fig. 3(d) as obtained by LFWT applied to s - T model. The intensity is represented by line thickness as in Fig. 2(b) with blue indicating the out-of-plane zz component and gray the in-plane components. The inset shows the Brillouin zone path. (b) zz susceptibility for the point D calculated using linear spin-wave theory applied to the corresponding TFIM with $J_z \approx 30$ meV and $h \approx 19$ meV. Cartoons capture the two distinct excitations – low-energy fluctuations of the in-plane pseudospins and high-energy Ising-type excitations.

of in-plane pseudospins. Its dispersion, soft near K , is approximately given by $\omega_{\mathbf{q}} \approx h[1 - (h/h_c)|\gamma_{\mathbf{q}}|^2]$ with $\gamma_{\mathbf{q}} = 2 \cos(\frac{\sqrt{3}}{2}q_x) + \exp(i\frac{3}{2}q_y)$ and $h_c = \frac{3}{2}J_z$ denoting the critical transverse field. Remarkably, this intense magnetic excitation stems from the moments that are magnetically invisible in the static pattern. In contrast to the triangular lattice case, the honeycomb spectrum [26] hosts only the Ising-type excitation and its low-energy part is empty.

Conclusions. We presented a detailed theoretical account on the exchange interactions in $4d^4$ and $5d^4$ spin-orbit Mott insulators in the regime of negative tetragonal or trigonal crystal field Δ . As illustrated by the corresponding phase diagrams and excitations for several 2D lattices, the low-energy magnetism can be well captured by AF transverse-field Ising model involving effective spins- $\frac{1}{2}$. Being based on d valence electrons, the emergent TFIM features convenient energy scales in the range of tens of meV. The transverse field is intrinsic, generated by CF itself, and is therefore sensitive to strain control. Robust Ising-type interactions are imposed by the internal spin-orbital structure of the d^4 ionic states,

and as such they are generic to both 180° and 90° bonding geometries. This universality of TFIM description is in strong contrast to the much different behavior of singlet-triplet models obtained for $\Delta/\zeta = 0$ in these two bonding-geometry cases [25, 27, 28]. The radical change of the magnetic model when varying Δ/ζ is an excellent illustration of the richness of the exchange interactions among $4d$ and $5d$ ions brought about by the complex structure of the low-energy ionic states. Apart from promising an identification/engineering of TFIM in the family of $4d$ and $5d$ correlated oxides, the proposed scenario also motivates the study of related theoretical issues. For example, the calculations suggest the dominant Ising exchange to be accompanied by small interactions between transverse components of effective spins. Their influence on the BKT behavior of TFIM is an interesting open problem.

Acknowledgments. Stimulating discussions with Giniyat Khaliullin are gratefully acknowledged. This work was supported by Czech Science Foundation (GAČR) under Project No. GA22-28797S.

-
- [1] P. G. de Gennes, Collective motions of hydrogen bonds, *Solid State Comm.* **1**, 132 (1963).
 - [2] S. Sachdev, *Quantum Phase Transitions* (Cambridge University Press, Cambridge, UK, 2011).
 - [3] A. Dutta, G. Aeppli, B. K. Chakrabarti, U. Divakaran, T. F. Rosenbaum, and D. Sen, *Quantum Phase Transitions in Transverse Field Spin Models: From Statistical Physics to Quantum Information* (Cambridge University Press, Cambridge, UK, 2015).
 - [4] E. Ising, Beitrag zur Theorie des Ferromagnetismus, *Z. Physik* **31**, 253 (1925).
 - [5] L. Onsager, Crystal Statistics. I. A Two-Dimensional Model with an Order-Disorder Transition, *Phys. Rev.* **65**, 117 (1944).
 - [6] B. Kaufman, Crystal Statistics. II. Partition Function Evaluated by Spinor Analysis, *Phys. Rev.* **76**, 1232 (1949).
 - [7] B. Kaufman and L. Onsager, Crystal Statistics.
 - [8] G. H. Wannier, Antiferromagnetism. The Triangular Ising Net, *Phys. Rev.* **79**, 357 (1950).
 - [9] G. H. Wannier, Erratum: Antiferromagnetism. The Triangular Ising Net, *Phys. Rev. B* **7**, 5017 (1973).
 - [10] C. Castellano, S. Fortunato, and V. Loreto, Statistical physics of social dynamics, *Rev. Mod. Phys.* **81**, 591 (2009).
 - [11] D. Sornette, Physics and financial economics (1776–2014): puzzles, Ising and agent-based models, *Rep. Prog. Phys.* **77**, 062001 (2014).
 - [12] R. Moessner, S. L. Sondhi, and P. Chandra, Two-Dimensional Periodic Frustrated Ising Models in a Transverse Field, *Phys. Rev. Lett.* **84**, 4457 (2000).
 - [13] R. Moessner and S. L. Sondhi, Ising models of quantum frustration, *Phys. Rev. B* **63**, 224401 (2001).
 - [14] S. V. Isakov and R. Moessner, Interplay of quantum and

- thermal fluctuations in a frustrated magnet, *Phys. Rev. B* **68**, 104409 (2003).
- [15] R. B. Stinchcombe, Ising model in a transverse field. I. Basic theory, *J. Phys. C: Solid State Phys.* **6**, 2459 (1973).
- [16] R. Coldea, D. A. Tennant, E. M. Wheeler, E. Wawrzynska, D. Prabhakaran, M. Telling, K. Habicht, P. Smeibidl, and K. Kiefer, Quantum Criticality in an Ising Chain: Experimental Evidence for Emergent E_8 Symmetry, *Science* **327**, 177 (2010).
- [17] H. Li, Y. D. Liao, B.-B. Chen, X.-T. Zeng, X.-L. Sheng, Y. Qi, Z. Y. Meng, and W. Li, Kosterlitz-Thouless melting of magnetic order in the triangular quantum Ising material TmMgGaO_4 , *Nature Comms.* **11**, 1111 (2020).
- [18] Z. Hu, Z. Ma, Y.-D. Liao, H. Li, C. Ma, Y. Cui, Y. Shang-guan, Z. Huang, Y. Qi, W. Li, Z. Y. Meng, J. Wen, and W. Yu, Evidence of the Berezinskii-Kosterlitz-Thouless phase in a frustrated magnet, *Nature Comms.* **11**, 5631 (2020).
- [19] Z. Dun, M. Daum, R. Baral, H. E. Fischer, H. Cao, Y. Liu, M. B. Stone, J. A. Rodriguez-Rivera, E. S. Choi, Q. Huang, H. Zhou, M. Mourigal, and B. A. Frandsen, Neutron scattering investigation of proposed Kosterlitz-Thouless transitions in the triangular-lattice Ising antiferromagnet TmMgGaO_4 , *Phys. Rev. B* **103**, 064424 (2021).
- [20] Y. Shen, C. Liu, Y. Qin, S. Shen, Y.-D. Li, R. Bewley, A. Schneidewind, G. Chen, and J. Zhao, Intertwined dipolar and multipolar order in the triangular-lattice magnet TmMgGaO_4 , *Nature Comms.* **10**, 4530 (2019).
- [21] C. Liu, F.-Y. Li, and G. Chen, Upper branch magnetism in quantum magnets: Collapses of excited levels and emergent selection rules, *Phys. Rev. B* **99**, 224407 (2019).
- [22] G. Chen, Intrinsic transverse field in frustrated quantum Ising magnets: Physical origin and quantum effects, *Phys. Rev. Research* **1**, 033141 (2019).
- [23] C. Liu, C.-J. Huang, and G. Chen, Intrinsic quantum Ising model on a triangular lattice magnet TmMgGaO_4 , *Phys. Rev. Research* **2**, 043013 (2020).
- [24] T. Takayama, J. Chaloupka, A. Smerald, G. Khaliullin, and H. Takagi, Spin-Orbit-Entangled Electronic Phases in $4d$ and $5d$ Transition-Metal Compounds, *J. Phys. Soc. Jpn.* **90**, 062001 (2021).
- [25] G. Khaliullin, Excitonic Magnetism in Van Vleck-type d^4 Mott Insulators, *Phys. Rev. Lett.* **111**, 197201 (2013).
- [26] See Supplemental Material for additional technical details and susceptibility spectra. It includes Refs. [24, 25, 28, 29, 31–35].
- [27] P. S. Anisimov, F. Aust, G. Khaliullin, and M. Daghofer, Nontrivial Triplon Topology and Triplon Liquid in Kitaev-Heisenberg-type Excitonic Magnets, *Phys. Rev. Lett.* **122**, 177201 (2019).
- [28] J. Chaloupka and G. Khaliullin, Highly frustrated magnetism in relativistic d^4 Mott insulators: Bosonic analog of the Kitaev honeycomb model, *Phys. Rev. B* **100**, 224413 (2019).
- [29] A. Jain, M. Krautloher, J. Porras, G. H. Ryu, D. P. Chen, D. L. Abernathy, J. T. Park, A. Ivanov, J. Chaloupka, G. Khaliullin, B. Keimer, and B. J. Kim, Higgs mode and its decay in a two-dimensional antiferromagnet, *Nature Phys.* **13**, 633 (2017).
- [30] S.-M. Souliou, J. Chaloupka, G. Khaliullin, G. Ryu, A. Jain, B. J. Kim, M. Le Tacon, and B. Keimer, Raman Scattering from Higgs Mode Oscillations in the Two-Dimensional Antiferromagnet Ca_2RuO_4 , *Phys. Rev. Lett.* **119**, 067201 (2017).
- [31] N. Papanicolaou, Pseudospin approach for planar ferromagnets, *Nucl. Phys. B* **240**, 281 (1984).
- [32] N. Papanicolaou, Unusual phases in quantum spin-1 systems, *Nucl. Phys. B* **305**, 367 (1988).
- [33] A. V. Chubukov, Fluctuations in spin nematics, *J. Phys.: Condens. Matter* **2**, 1593 (1990).
- [34] A. Joshi, M. Ma, F. Mila, D. N. Shi, and F. C. Zhang, Elementary excitations in magnetically ordered systems with orbital degeneracy, *Phys. Rev. B* **60**, 6584 (1999).
- [35] T. Sommer, M. Vojta, and K. W. Becker, Magnetic properties and spin waves of bilayer magnets in a uniform field, *Eur. Phys. J. B* **23**, 329 (2001).
- [36] Y.-C. Wang, Y. Qi, S. Chen, and Z. Y. Meng, Caution on emergent continuous symmetry: A Monte Carlo investigation of the transverse-field frustrated Ising model on the triangular and honeycomb lattices, *Phys. Rev. B* **96**, 115160 (2017).
- [37] C.-J. Huang, L. Liu, Y. Jiang, and Y. Deng, Worm-algorithm-type simulation of the quantum transverse-field Ising model, *Phys. Rev. B* **102**, 094101 (2020).

Supplemental Material for
Emergent transverse-field Ising model in d^4 spin-orbit Mott insulators

Jiří Chaloupka

*Department of Condensed Matter Physics, Faculty of Science,
 Masaryk University, Kotlářská 2, 61137 Brno, Czech Republic*

A. LOW-ENERGY MULTIPLY STATES OF t_{2g}^4 CONFIGURATION

To construct the multiplet states forming the low-energy basis, we consider t_{2g}^4 states corresponding to two holes made in the fully populated t_{2g}^6 configuration. Working within the LS coupling scheme, we limit ourselves to the sector with maximum total spin $S = 1$ of the hole pair which is favored by Hund's coupling. The total t_{2g} orbital momentum of the hole pair is restricted to $L = 1$ in that case. The nine-fold degeneracy of the $S = L = 1$ sector is lifted by a simultaneous action of spin-orbit coupling (SOC)

$$\mathcal{H}_{\text{SOC}} = \frac{\zeta}{2S} \mathbf{S} \cdot \mathbf{L} \quad (1)$$

and tetragonal or trigonal crystal-field (CF) that splits the single-electron t_{2g} levels. In the tetragonal case with the CF axis being one of the main octahedral axes, the splitting takes a simple form diagonal in the conventional t_{2g} orbital basis, for example $\mathcal{H}_{\text{CF}} = \frac{1}{3}\Delta (d_{yz}^\dagger d_{yz} + d_{zx}^\dagger d_{zx} - 2d_{xy}^\dagger d_{xy})$ if the CF axis coincides with z . \mathcal{H}_{CF} for the hole pair may be compactly expressed using the component of total \mathbf{L} parallel to the CF axis:

$$\mathcal{H}_{\text{CF}} = \Delta (L_z^2 - \frac{2}{3}). \quad (2)$$

The case of the trigonal splitting is a bit more complicated, involving so-called a_{1g} e'_g orbital combinations, but Eq. (2) remains valid if we again associate the axis z with the CF axis, i.e. $z \parallel [111]$ in the octahedral reference frame as shown in Fig. 1 of the main text.

The Hamiltonian $\mathcal{H}_{\text{SOC}} + \mathcal{H}_{\text{CF}}$ is easily diagonalized giving rise to the excitation energies plotted in Fig. S1(a). In the case of $\Delta/\zeta = 0$ where only \mathcal{H}_{SOC} contributes, the energy eigenstates correspond to $J = 0, 1, 2$ eigenstates of the total angular momentum $\mathbf{J} = \mathbf{L} + \mathbf{S}$ as evident from the rearrangement $\mathbf{S} \cdot \mathbf{L} = \frac{1}{2}(\mathbf{J}^2 - \mathbf{L}^2 - \mathbf{S}^2)$. In the general case, the energy eigenstates can be conveniently formulated in terms of the states $|L_z, S_z\rangle$ that simultaneously diagonalize the out-of-plane components of the total t_{2g} orbital momentum and the total spin. Thanks to the identical form (2) for both tetragonal and trigonal splitting, all the following expressions are universal, differing just in the interpretation of the z axis. The singlet ionic ground state s is given by

$$|s\rangle = \frac{1}{\sqrt{2}}(|+1, -1\rangle + |-1, +1\rangle) \cos \vartheta_0 - |0, 0\rangle \sin \vartheta_0 \quad (3)$$

with the auxiliary angle obeying $\tan 2\vartheta_0 = 2\sqrt{2}/(1 - 2\delta)$ where $\delta = \Delta/\zeta$ measures the relative strength of CF versus SOC. This angle is plotted in Fig. 1(d) of the main text using the same horizontal axis as that used in Fig. S1. First three excited states forming degenerate $J = 1$ triplet at $\Delta/\zeta = 0$ split into an isolated state

$$|T_z\rangle = \frac{i}{\sqrt{2}}(|+1, -1\rangle - |-1, +1\rangle) \quad (4)$$

independent on Δ/ζ and the degenerate pair

$$|T_{\pm 1}\rangle = \pm |0, \pm 1\rangle \sin \vartheta_1 \mp |\pm 1, 0\rangle \cos \vartheta_1 \quad (5)$$

that we rearrange into Cartesian combinations

$$|T_x\rangle = \frac{i}{\sqrt{2}}(|T_{+1}\rangle - |T_{-1}\rangle), \quad (6)$$

$$|T_y\rangle = \frac{1}{\sqrt{2}}(|T_{+1}\rangle + |T_{-1}\rangle). \quad (7)$$

Here the auxiliary angle ϑ_1 fulfills the equation $\tan \vartheta_1 = 1/(\sqrt{1 + \delta^2} - \delta)$. A practical advantage of the Cartesian $T_{x,y,z}$ is their direct link to the components of the magnetic moment to be discussed later. The remaining five states corresponding to $J = 2$ quintuplet at $\Delta/\zeta = 0$ are at high energies, completely omitted from our model and we thus do not list them explicitly here.

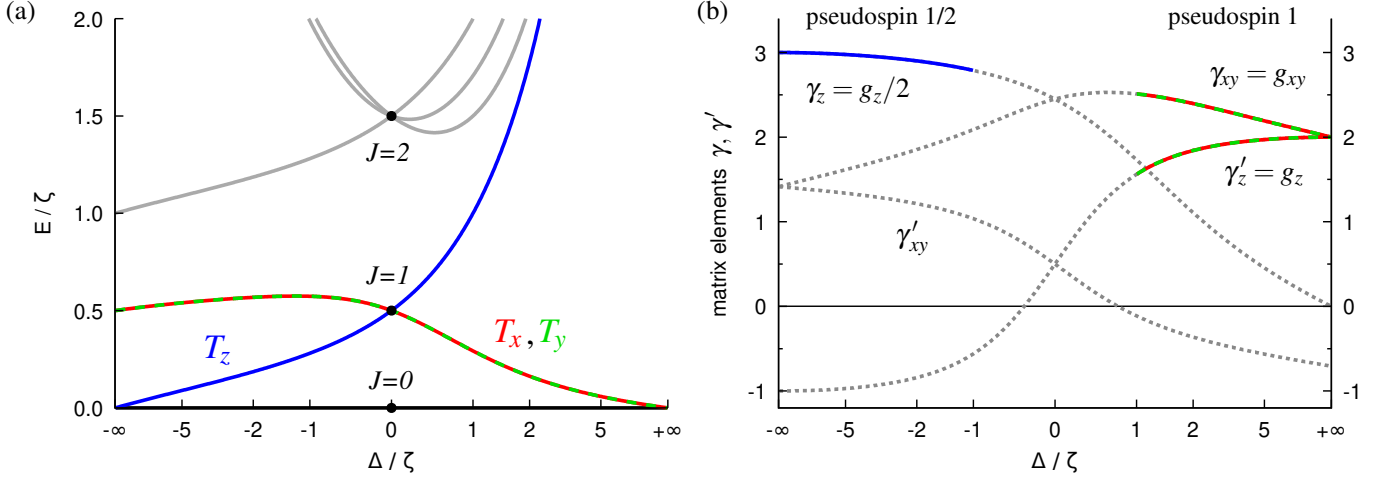


FIG. S1. (a) Ionic excitation energies obtained within LS coupling scheme for the $S = 1, L = 1$ sector of t_{2g}^4 favored by Hund's coupling. Plotted are the energies relative to the ground-state singlet level. At $\Delta/\zeta = 0$, the multiplet states are eigenstates of the total angular momentum $\mathbf{J} = \mathbf{L} + \mathbf{S}$. (b) Factors entering the operators of the magnetic moment in (11), (12), (13). In the $\Delta \lesssim -\zeta$ regime, the low-energy pair of states s and T_z maps to pseudospin- $\frac{1}{2}$ with zero in-plane g -factor $g_{xy} = 0$ and large out-of-plane $g_z = 2\gamma_z$. In the $\Delta \gtrsim +\zeta$ regime, the low-energy states s, T_x, T_y form pseudospin-1 with the g -factors $g_{xy} = \gamma_{xy}$ and $g_z = \gamma'_z$, both approaching 2 in the large- Δ limit where L is quenched leaving only the spin component active.

The energies of the relevant ionic states obtained by diagonalizing $\mathcal{H}_{\text{SOC}} + \mathcal{H}_{\text{CF}}$

$$E_s/\zeta = -\frac{1}{4} \left[1 + \sqrt{(1-2\delta)^2 + 8} \right] - \frac{1}{6}\delta, \quad (8)$$

$$E_{T_z}/\zeta = -\frac{1}{2} + \frac{1}{3}\delta, \quad (9)$$

$$E_{T_{x,y}}/\zeta = -\frac{1}{2}\sqrt{1 + \delta^2} - \frac{1}{6}\delta \quad (10)$$

are plotted in Fig. S1(a) relative to the ground-state energy E_s . As Fig. S1(a) suggests, the selection of T states to be included in the local basis for a low-energy magnetic model depends on the Δ/ζ ratio. In our regime of interest, $\Delta \lesssim -\zeta$, the state T_z is singled out as the first excited state and together with s it forms a reduced two-dimensional basis that can be captured by a pseudospin- $\frac{1}{2}$. For roughly $|\Delta| \lesssim \zeta$, one needs to treat all T states on an equal footing, leading to the four-dimensional basis spanned by s, T_x, T_y, T_z . We have actually used this largest basis in most calculations in the paper for the purpose of checking the validity of the simplified pseudospin- $\frac{1}{2}$ model in the regime $\Delta \lesssim -\zeta$. Finally, for $\Delta \gtrsim +\zeta$, T_z is quickly lifted up and the three remaining states s, T_x, T_y are sufficient to capture the low-energy magnetism. In this case, they can be mapped to a pseudospin-1.

Before discussing the two pseudospin regimes in detail, let us specify the operators of the magnetic moment carried by the four states s, T_α ($\alpha = x, y, z$). These operators were heavily used in our calculations to characterize the magnetic phases in terms of static magnetic structure and magnetic excitation spectra. They are obtained by evaluating the matrix elements of the general magnetic moment operator $\mathbf{M} = 2\mathbf{S} - \mathbf{L}$ between the four ionic states (note the negative sign of effective t_{2g} orbital momentum contribution as compared to the real \mathbf{L}). Expressed via the corresponding creation and annihilation operators, the magnetic moment components take the form

$$M_x = \gamma_{xy} (-i)(s^\dagger T_x - T_x^\dagger s) + \gamma'_{xy} (-i)(T_y^\dagger T_z - T_z^\dagger T_y), \quad (11)$$

$$M_y = \gamma_{xy} (-i)(s^\dagger T_y - T_y^\dagger s) + \gamma'_{xy} (-i)(T_z^\dagger T_x - T_x^\dagger T_z), \quad (12)$$

$$M_z = \gamma_z (-i)(s^\dagger T_z - T_z^\dagger s) + \gamma'_z (-i)(T_x^\dagger T_y - T_y^\dagger T_x). \quad (13)$$

Each component M_α has a Van Vleck-type contribution residing on a transition between s and T_α states, and a contribution originating solely within the T -sector. The prefactors entering M_α read as

$$\gamma_{xy} = \cos \vartheta_0 (\sqrt{2} \cos \vartheta_1 + \frac{1}{\sqrt{2}} \sin \vartheta_1) + \sin \vartheta_0 (\cos \vartheta_1 + 2 \sin \vartheta_1), \quad (14)$$

$$\gamma'_{xy} = \sqrt{2} \cos \vartheta_1 - \frac{1}{\sqrt{2}} \sin \vartheta_1, \quad (15)$$

$$\gamma_z = 3 \cos \vartheta_0, \quad (16)$$

$$\gamma'_z = 2 - 3 \cos^2 \vartheta_1 \quad (17)$$

and are plotted in Fig. S1(b) for the full range of Δ/ζ . As expected, in the cubic limit $\Delta/\zeta = 0$ where there is no preference among the T states, the factors partially coincide

$$\Delta/\zeta = 0: \quad \gamma_{xy} = \gamma_z = \sqrt{6} \quad \text{and} \quad \gamma'_{xy} = \gamma'_z = \frac{1}{2} \quad (18)$$

so that the magnetic moment components get unified to

$$\mathbf{M} = \sqrt{6}(-i)(s^\dagger \mathbf{T} - \mathbf{T}^\dagger s) + \frac{1}{2}(-i)(\mathbf{T}^\dagger \times \mathbf{T}). \quad (19)$$

Negative Δ : pseudospin- $\frac{1}{2}$ case

To capture the low-energy magnetic behavior in the $\Delta \lesssim -\zeta$ regime, it is sufficient to use the two-dimensional basis consisting of s and T_z states. One of the fundamental parameters of the resulting model is the energy separation of these states, i.e. energy of T_z relative to s which evaluates to

$$E_T = E(T_z) - E(s) = \frac{1}{4}\zeta \left[\sqrt{(1-2\delta)^2 + 8} - (1-2\delta) \right] = \frac{\zeta}{1-2\delta} \frac{2}{1 + \sqrt{1 + \frac{8}{(1-2\delta)^2}}} \approx \frac{\zeta}{1-2\delta}. \quad (20)$$

States from the two-dimensional space spanned by s and T_z can be described by pseudospin $\tilde{S} = \frac{1}{2}$ which can be introduced in a number of ways. A particularly convenient one that makes the magnetic model most transparent is based on pseudospin-up and down states defined as the linear combinations

$$|\tilde{\uparrow}\rangle = \frac{1}{\sqrt{2}}(|s\rangle + i|T_z\rangle) = c^2|-1, +1\rangle - s^2|+1, -1\rangle - \sqrt{2}cs|0, 0\rangle, \quad (21)$$

$$|\tilde{\downarrow}\rangle = \frac{1}{\sqrt{2}}(|s\rangle - i|T_z\rangle) = c^2|+1, -1\rangle - s^2|-1, +1\rangle - \sqrt{2}cs|0, 0\rangle \quad (22)$$

where $c = \cos \frac{\vartheta_0}{2}$ and $s = \sin \frac{\vartheta_0}{2}$. The pseudospin operators are then connected to the s and T_z operators as follows:

$$\tilde{S}_x = \frac{1}{2} - n_{T_z}, \quad \tilde{S}_y = \frac{1}{2}(s^\dagger T_z + T_z^\dagger s), \quad \tilde{S}_z = -\frac{i}{2}(s^\dagger T_z - T_z^\dagger s). \quad (23)$$

In this formulation, the energy cost of having T_z on a given site which is measured by $E_T n_{T_z}$ with $n_{T_z} = T_z^\dagger T_z$ translates to a transverse-field term $-E_T \tilde{S}_x$. The magnetic moment carried by the pseudospin \tilde{S} is easily obtained by dropping all the $T_{x,y}$ terms in (11)–(13) which leaves us with

$$M_x = 0, \quad M_y = 0, \quad M_z = \gamma_z(-i)(s^\dagger T_z - T_z^\dagger s). \quad (24)$$

A comparison with $(M_x, M_y, M_z) = (g_{xy}\tilde{S}_x, g_{xy}\tilde{S}_y, g_z\tilde{S}_z)$ yields zero in-plane g -factor $g_{xy} = 0$ and large out-of-plane $g_z = 2\gamma_z$ reaching the value of 6 in $\Delta \rightarrow -\infty$ limit.

Positive Δ : pseudospin-1 case

Though it is not directly used in the main text, for completeness we also describe the mapping of the basis s , T_x , T_y relevant at large positive Δ/ζ to pseudospin-1. In this case, the following relations link pseudospin-1 operators and s , $T_{x,y}$ operators:

$$\tilde{S}_x = -i(s^\dagger T_x - T_x^\dagger s), \quad \tilde{S}_y = -i(s^\dagger T_y - T_y^\dagger s), \quad \tilde{S}_z = -i(T_x^\dagger T_y - T_y^\dagger T_x). \quad (25)$$

The energy splitting between s and $T_{x,y}$ states expressed via $E_T(n_{T_x} + n_{T_y})$ with

$$E_T = E(T_{x,y}) - E(s) = \frac{1}{4}\zeta \left[1 + \sqrt{(1-2\delta)^2 + 8} - 2\sqrt{1 + \delta^2} \right] \quad (26)$$

translates now to a single-ion anisotropy term $E_T \tilde{S}_z^2$. By removing T_z parts in (11)–(13), we get the projected magnetic moment operators

$$M_x = \gamma_{xy}(-i)(s^\dagger T_x - T_x^\dagger s), \quad M_y = \gamma_{xy}(-i)(s^\dagger T_y - T_y^\dagger s), \quad M_z = \gamma'_z(-i)(T_x^\dagger T_y - T_y^\dagger T_x). \quad (27)$$

that immediately give the pseudospin-1 g -factors $g_{xy} = \gamma_{xy}$ and $g_z = \gamma'_z$. Both of them approach the value of 2 in the $\Delta \rightarrow +\infty$ limit where the orbital contribution to the magnetic moment is fully quenched and the pseudospin corresponds to a pure spin-1.

B. PARAMETERS OF THE PSEUDOSPIN- $\frac{1}{2}$ MODEL

The pseudospin- $\frac{1}{2}$ model has been derived by evaluating the exchange interactions originating from nearest-neighbor electronic hopping utilizing standard second-order perturbation theory. The initial and final bond states were composed from pseudospin- $\frac{1}{2}$ states (21) and (22) discussed in Sec. A. The energies of the virtual states were evaluated using the Hubbard-Kanamori Hamiltonian including the usual intra and interorbital Coulomb interaction (U , $U' = U - 2J_H$) and Hund's coupling (J_H) terms

$$\mathcal{H}_{\text{Coulomb}} = U \sum_{\alpha} n_{\alpha\uparrow} n_{\alpha\downarrow} + \sum_{\alpha < \beta} (U' - \frac{1}{2} J_H) n_{\alpha} n_{\beta} - 2 \sum_{\alpha < \beta} J_H \mathbf{S}_{\alpha} \cdot \mathbf{S}_{\beta} + \sum_{\alpha \neq \beta} J_H \alpha_{\uparrow}^{\dagger} \alpha_{\downarrow}^{\dagger} \beta_{\downarrow} \beta_{\uparrow} \quad (28)$$

and neglecting the effects of ζ and Δ . Only purely t_{2g} electron configurations were included in the virtual states. In Eq. (28), α, β run through the t_{2g} orbitals and $n_{\alpha\sigma}$ ($\sigma = \uparrow, \downarrow$), $n_{\alpha} = \sum_{\sigma} n_{\alpha\sigma}$ count the corresponding electron occupations.

In the case of 180° bond geometry, the hopping involves two active orbitals selected by the bond direction and connected diagonally. For the bonds along x and y direction present in the square lattice, we have (spin summation is implied):

$$\mathcal{H}_t^{(x)} = -t (d_{xy}^{\dagger} d_{xy} + d_{zx}^{\dagger} d_{zx})_{ij} + \text{H.c.}, \quad \mathcal{H}_t^{(y)} = -t (d_{xy}^{\dagger} d_{xy} + d_{yz}^{\dagger} d_{yz})_{ij} + \text{H.c.} \quad (29)$$

In the case of 90° bond geometry encountered for honeycomb and triangular lattice, two complementary nearest-neighbor hopping channels need to be considered. For convenience, we use here the octahedral reference frame instead of the one shown in Fig. 1(e). On a z -bond which is defined by a metal₂-O₂ plaquette perpendicular to the z axis (see e.g. Fig. 5 of Ref. [24] for a sketch of the hopping geometry), the hopping reads as

$$\mathcal{H}_{tt'}^{(z)} = t (d_{zx}^{\dagger} d_{yz} + d_{yz}^{\dagger} d_{xz})_{ij} - t' (d_{xy}^{\dagger} d_{xy})_{ij} + \text{H.c.} \quad (30)$$

The hopping Hamiltonians for the other two bond directions are obtained by cyclic permutation among x, y, z .

The derivation for both bond geometries gives the following form of the pseudospin- $\frac{1}{2}$ model with bond-independent interactions [we are now switching back to the reference frame of Fig. 1(e)]

$$\mathcal{H}_{\tilde{S}} = \sum_{\langle ij \rangle} \left(J_z \tilde{S}_i^z \tilde{S}_j^z + J_x \tilde{S}_i^x \tilde{S}_j^x + J_y \tilde{S}_i^y \tilde{S}_j^y \right) - (h + \delta h) \sum_i \tilde{S}_i^x. \quad (31)$$

The expressions for the exchange constants J_{α} and the correction δh to the transverse field $h = E_T$ can be cast into a universal structure emphasizing the CF splitting dependence via the auxiliary angle ϑ_0 entering (21) and (22):

$$J_z = \frac{1}{U_{\text{red}}} (A_1 + A_2 \sin^2 \vartheta_0), \quad (32)$$

$$J_y = \frac{1}{U_{\text{red}}} A_3 \sin^2 \vartheta_0, \quad (33)$$

$$J_x - J_y = \frac{1}{U_{\text{red}}} A_4 \sin^4 \vartheta_0, \quad (34)$$

$$\delta h = \frac{1}{U_{\text{red}}} (A_5 + A_6 \sin^2 \vartheta_0) \sin^2 \vartheta_0, \quad (35)$$

where we have adopted a shorthand notation $U_{\text{red}} = U(1 - 3\eta)(1 + 2\eta)$ and $\eta = J_H/U$. In the $\Delta \lesssim -\zeta$ regime, the factor $\sin^2 \vartheta_0$ is small, vanishing in the $\Delta \rightarrow -\infty$ limit and its asymptotic Δ -dependence is captured by an expansion $\sin^2 \vartheta_0 = 2\varepsilon^2 - 12\varepsilon^4 + \mathcal{O}(\varepsilon^6)$ with the small parameter $\varepsilon = 1/(1 - 2\delta)$. The quantities A_1 to A_6 containing various combinations of the hopping amplitudes and η measuring the relative strength of Hund's coupling are listed below. Note that being collected at the bonds attached to a given site, the exchange correction δh to the local term depends on the number of nearest neighbors z for the given lattice.

- 180° bonds (square lattice with $z=4$)

$$A_1 = (5 - 12\eta - 19\eta^2) t^2, \quad (36)$$

$$A_2 = -4(1 - 3\eta - 5\eta^2) t^2, \quad (37)$$

$$A_3 = (1 + 2\eta - 5\eta^2) t^2, \quad (38)$$

$$A_4 = \frac{1}{4}(1 + 12\eta + 15\eta^2) t^2, \quad (39)$$

$$A_5 = -(1 - 6\eta - 11\eta^2) t^2, \quad (40)$$

$$A_6 = -\frac{1}{2}(1 + 12\eta + 15\eta^2) t^2. \quad (41)$$

- 90° bonds ($A_{5,6}$ apply to the honeycomb lattice with $z=3$, they are two times larger for the $z=6$ triangular lattice)

$$A_1 = \frac{4}{9}[(7 - 27\eta - 47\eta^2)t^2 + 2(1 + 3\eta + 7\eta^2)tt' + 4(1 - 3\eta - 5\eta^2)t'^2], \quad (42)$$

$$A_2 = -\frac{2}{3}[(5 - 18\eta - 31\eta^2)t^2 + (1 + 4\eta + 9\eta^2)tt' + 2(1 - 4\eta - 7\eta^2)t'^2], \quad (43)$$

$$A_3 = -\frac{2}{3}(1 + 2\eta - 5\eta^2)t(t + t'), \quad (44)$$

$$A_4 = (1 + 3\eta - 3\eta^2)t^2 - 2\eta(1 + 2\eta)tt', \quad (45)$$

$$A_5 = (1 + 3\eta - 3\eta^2)t^2 + (1 - 9\eta^2)tt', \quad (46)$$

$$A_6 = -\frac{3}{2}(1 + 3\eta - 3\eta^2)t^2 + 3\eta(1 + 2\eta)tt'. \quad (47)$$

C. UNDERLYING HARDCORE BOSON MODELS, MAPPING TO PSEUDOSPIN- $\frac{1}{2}$ MODEL

The full s - T model for arbitrary Δ was obtained by the same type of calculation as described in Sec. B but considering now all combinations of four local basis states $|s\rangle$, $|T_\alpha\rangle$ ($\alpha = x, y, z$) on a bond. This amounts to connecting 16 initial bond states to 16 final bond states by the exchange Hamiltonian to be constructed, giving 256 possible bond processes in total. The model Hamiltonian is too complex to be presented explicitly here, but its general structure is of the form

$$\mathcal{H}_{s-T} = \sum_i E_m \Psi_{mi}^\dagger \Psi_{mi} + \sum_{\langle ij \rangle} V_{mm'nn'} \Psi_{mi}^\dagger \Psi_{m'j}^\dagger \Psi_{ni} \Psi_{n'j} \quad (48)$$

involving four-component vector bosons $\Psi = (s, T_x, T_y, T_z)$ subject to local hardcore constraint $n_s + n_{T_x} + n_{T_y} + n_{T_z} = 1$ at each site (here $n_s = s^\dagger s$, $n_{T_x} = T_x^\dagger T_x$ etc.). Summation over indices $m, m', n, n' = 0, 1, 2, 3$ is implied. The on-site excitation energies E_m are given by the multiplet levels as in (20) and (26), potentially supplemented by negligible exchange corrections. The amplitudes $V_{mm'nn'}$ are functions of t, t', U, J_H and the auxiliary angles ϑ_0, ϑ_1 . The corresponding expressions would be similar to those presented in Sec. B but more complex. Moreover, they depend on the direction of the particular bond $\langle ij \rangle$ since the bond-directional states T_x, T_y are included.

In the $\Delta \lesssim -\zeta$ regime, it is sufficient to employ a much simpler hardcore boson model obtained by a projection of (48) onto s, T_z subspace. The exchange interactions in this reduced model are fully captured by only a few terms – hopping of T_z particles, their pairwise creation and annihilation, and their repulsion or attraction. Including a small correction to s - T_z splitting E_T due to exchange processes, the resulting Hamiltonian reads as

$$\mathcal{H}_{s-T_z} = \sum_{\langle ij \rangle} \left\{ \tau [(T_z^\dagger s)_i (s^\dagger T_z)_j + \text{H.c.}] - \kappa [(T_z^\dagger s)_i (T_z^\dagger s)_j + \text{H.c.}] + V n_{T_z i} n_{T_z j} \right\} + (E_T + \delta E_T) \sum_i n_{T_z i}. \quad (49)$$

The parameters τ, κ, V are independent on the bond direction since we projected out the states $T_{x,y}$ having bond-directional wave functions. By rewriting the terms of the above Hamiltonian using a new basis composed of $|\tilde{\uparrow}\rangle = \frac{1}{\sqrt{2}}(|s\rangle + i|T_z\rangle)$ and $|\tilde{\downarrow}\rangle = \frac{1}{\sqrt{2}}(|s\rangle - i|T_z\rangle)$, the s - T_z model can be mapped to the pseudospin- $\frac{1}{2}$ model (31). This way one finds the relations connecting the two formulations in terms of parameters

$$J_x = V, \quad J_y = 2(\tau - \kappa), \quad J_z = 2(\tau + \kappa), \quad \delta h = \delta E_T + \frac{1}{2}zV \quad (50)$$

and giving identical expressions for $J_{x,y,z}$ and δh as (32)–(35) obtained by working out the second order perturbation theory directly in the $|\tilde{\uparrow}\rangle, |\tilde{\downarrow}\rangle$ basis.

D. PHASE DIAGRAMS AND EXCITATION SPECTRA AT A HARMONIC LEVEL

To establish approximate phase diagrams of the above hardcore boson models, we use a simple variational approach based on factorized trial states. For the full s - T model (48) or the projected s - T_z model (49) [equivalent to the pseudospin- $\frac{1}{2}$ model (31)], we use

$$|\text{trial}\rangle = \prod_i \left(\sqrt{1 - \rho_i} s^\dagger + \sqrt{\rho_i} \sum_\alpha d_{i\alpha}^* T_{i\alpha}^\dagger \right) |\text{vac}\rangle \quad \text{or} \quad \prod_i \left(\sqrt{1 - \rho_i} s^\dagger + \sqrt{\rho_i} e^{i\phi_i} T_{iz}^\dagger \right) |\text{vac}\rangle, \quad (51)$$

respectively. These enable to assess the tendency of triplets to form a condensate and to determine the preferred condensate structure. We consider unit cells of various sizes and minimize the average value of the model Hamiltonian

with respect to position-dependent variational parameters ρ_i (“condensate density”) and either the complex vectors \mathbf{d}_i embedding direction and phases in the triplet space (s - \mathbf{T} model) or just the phases ϕ_i of T_z (s - T_z model). The resulting optimal configuration can be used to evaluate e.g. the magnetic structure via (11)–(13) or pseudospin structure via (23).

To determine the excitation spectra on a harmonic expansion level, we have adopted a variant of linear flavor wave theory (LFWT) [31–35] that proceeds according to the following recipe relevant for the s - \mathbf{T} model case. First, using the result of the previous minimization, a sublattice-dependent rotation among the bosonic operators (s, T_x, T_y, T_z) \rightarrow (c, a, b_1, b_2) is introduced to bring the optimal |trial) state to a simplified form

$$|\text{trial}\rangle = \prod_i c_i^\dagger |\text{vac}\rangle. \quad (52)$$

This requirement implies the first part of the transformation – the new boson c needs to be defined via the relation $c = \sqrt{1-\rho} s + \sqrt{\rho} \sum_\alpha d_\alpha T_\alpha$. Boson a is an orthogonal complement of c given by $a = \sqrt{\rho} s - \sqrt{1-\rho} \sum_\alpha d_\alpha T_\alpha$. It is constructed to maintain the \mathbf{d} structure and as such it is linked to an amplitude oscillation of the condensate. The remaining two bosons b_1 and b_2 are constructed by continuing the orthogonalization procedure which generates directions perpendicular to \mathbf{d} in the triplet space: $b_n = \sum_\alpha d_\alpha^{(n)} T_\alpha$ ($n = 1, 2$) with $\mathbf{d}^{(n)} \cdot \mathbf{d} = 0$ and $\mathbf{d}^{(1)} \cdot \mathbf{d}^{(2)} = 0$. Therefore, b_1 and b_2 carry two magnon-like modes altering primarily the magnetic structure of the condensate and not its amplitude. After the rotation is performed, the condensed combination of boson operators is replaced as $c, c^\dagger \rightarrow \sqrt{1-n_a-n_{b_1}-n_{b_2}}$ to approximately account for the hardcore constraint $n_s+n_T=n_c+n_a+n_b=1$ and the resulting Hamiltonian is expanded up to second order in boson operators providing a harmonic Hamiltonian involving three bosons a, b_1, b_2 per site in the unit cell. As the last step, this Hamiltonian is diagonalized via multiboson Bogoliubov transformation. The procedure for the s - T_z model is simpler as it does not involve the two bosons b_1 and b_2 . In principle, thanks to the equivalence of the two formulations (49) and (31), the excitation spectrum obtained within s - T_z model could be also accessed by solving the equivalent pseudospin- $\frac{1}{2}$ model. However, if the pseudospin- $\frac{1}{2}$ model is treated by linear spin-wave theory, there are slight quantitative differences since the constraints are handled differently and the two harmonic expansions are not identical.

Finally, the harmonic modes obtained using the above procedure and the associated matrix propagator can be used to evaluate the dynamic magnetic susceptibility

$$\chi_{\alpha\alpha}(\mathbf{q}, \omega) = i \int_0^\infty \langle [M_\alpha(\mathbf{q}, t) M_\alpha(-\mathbf{q}, 0)] \rangle e^{i(\omega+i0^+)t} dt \quad (53)$$

presented in the main text and the following section. Via the above bosonic rotation and a subsequent substitution for c, c^\dagger , the magnetic moment operator M_α can be expressed via the a, b_1 , and b_2 operators. Keeping only the linear terms in M_α , the susceptibility can be constructed from the components of the matrix propagator for the a, b_1 , and b_2 bosons.

E. ADDITIONAL MAGNETIC SUSCEPTIBILITY SPECTRA

Square lattice

Figure S2 presents sample magnetic excitation spectra obtained for the same parameter setup as in Fig. 2 of the main text. In addition to the three spectra for the A, B, C points with $\Delta < 0$ that were already shown in Fig. 2, here we cover also the positive Δ range to contrast the nature of magnetic excitations in these two cases. For $\Delta \gtrsim +\zeta$, the low-energy magnetic behavior can be roughly described by pseudospin-1 model

$$\mathcal{H}_{\tilde{S}} = \sum_{\langle ij \rangle} \left[J_{xy} \left(\tilde{S}_i^x \tilde{S}_j^x + \tilde{S}_i^y \tilde{S}_j^y \right) + J_z \tilde{S}_i^z \tilde{S}_j^z \right] + E_T \sum_i (\tilde{S}_i^z)^2 \quad (54)$$

where the pseudospin-1 operators have been introduced in (25). The large single-ion anisotropy term pushes the pseudospins into the xy plane giving them specific dynamics manifesting itself by XY-type magnon dispersion [29].

The spectra shown in Fig. S2(b) are calculated using the LFWT for the s - \mathbf{T} model. If the LFWT is applied to the reduced models, either s - T_z (equivalent to pseudospin- $\frac{1}{2}$ model) or s - T_x - T_y (equivalent to pseudospin-1 model), the corresponding parts of the magnetic excitation spectra are exactly reproduced. This applies to the phases where the complementary bosons do not participate in condensation. Hence, on the level of LFWT, the s - T_z model fully captures the zz susceptibility in the PM phase and the left AF phase, covering the entire range of interest on both sides of the QCP. Similarly, the s - T_x - T_y model exactly reproduces the xx and yy susceptibility in the PM phase and the right AF phase.

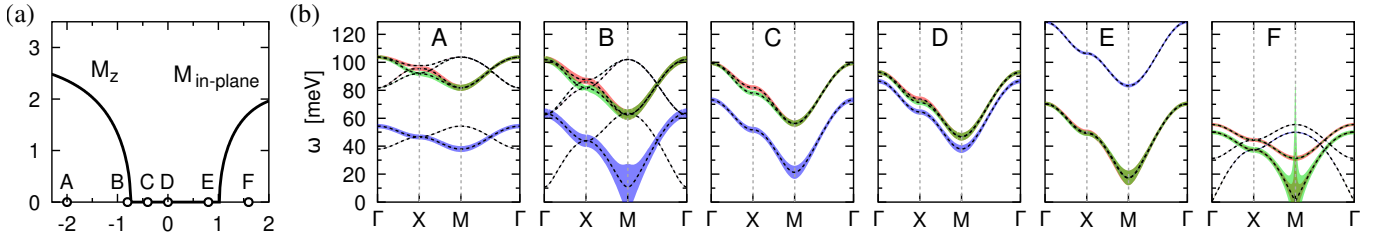


FIG. S2. Sample magnetic excitation spectra covering both the negative and positive Δ parts of the phase diagram in Fig. 2(a) of the main text [reproduced in (a)]. One can clearly see the distinct fate of the xx , yy (red and green) and zz (blue) modes on the two sides of the $\Delta = 0$ point D, where they are quasidegenerate. While flat Ising-type excitations are observed on the left for $\Delta < 0$ after the AF order develops (point A), at $\Delta > 0$ on the right, T_z is quickly lifted up and the low-energy behavior is captured by effective spin-1 model where exchange interactions of predominantly XY-type compete with varying single-ion anisotropy [24, 29]. In the ordered regime it features nearly gapless magnons and a gapful amplitude mode (point F). The approaching QCP is generally signaled by a characteristic soft mode that touches zero energy at QCP (near points B and E).

Honeycomb lattice

The excitation spectra complementing the $\Delta < 0$ phase diagram of the honeycomb model presented in Fig. 3(c) of the main text are shown in Fig. S3. Since the honeycomb lattice does not suffer from the geometric frustration, the picture is rather simple. As we drive the system from PM to AF phase, the excitations first soften at the AF momentum $\mathbf{q} = \Gamma'$, harden back after passing through the QCP, and finally become Ising-like with a flat dispersion as we get deeper into the AF phase. The overall behavior is thus very similar to that observed in the previous paragraph for the square lattice. A comparison of Fig. S3(c) and Fig. S3(d) shows that the relevant out-of-plane magnetic modes entering zz component of the magnetic susceptibility are well captured by the reduced s - T_z Hamiltonian equivalent to the pseudospin- $\frac{1}{2}$ model.

This point is elaborated further in Fig. S4 where we systematically cover the phase diagram of Fig. S3(a) focusing solely on the zz component of the magnetic susceptibility with the aim to test the pseudospin- $\frac{1}{2}$ model. We can observe a good match between the results of the s - \mathbf{T} model and s - T_z model for $\Delta \lesssim -\zeta$, which is the domain of applicability of the reduced model, and the agreement is rather good even at $\Delta/\zeta = -0.5$ if t' is comparable or larger than t (i.e. $\beta \geq 0.4$ in our plots). As in the case of the square lattice, this suggests the availability of TFIM-like physics on both sides of QCP. However, in contrast to the square-lattice case, the harmonic χ_{zz} spectra obtained for

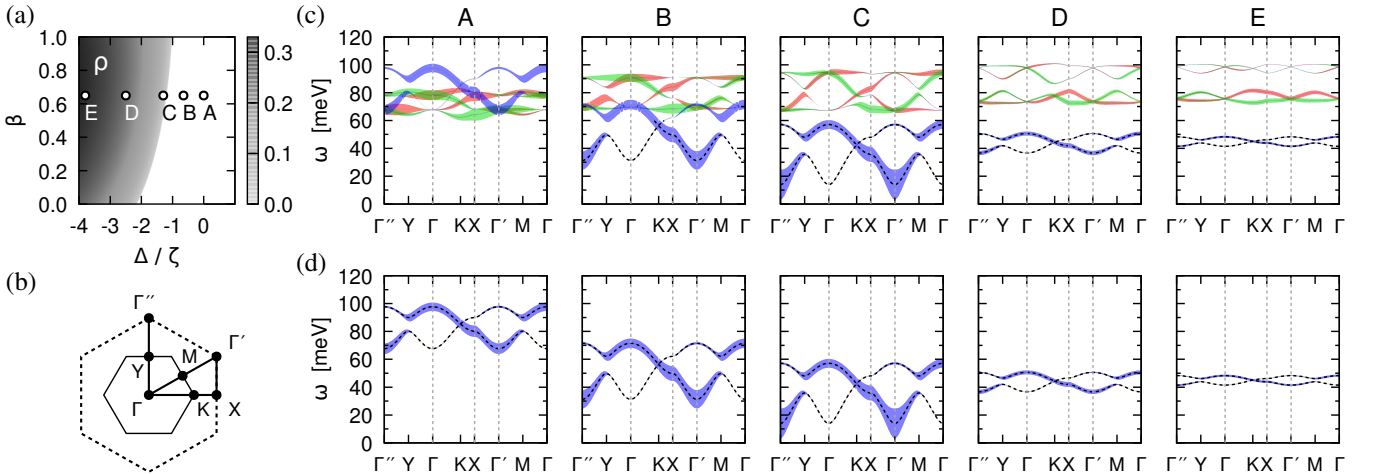


FIG. S3. Magnetic excitation spectra for a set of points in the honeycomb phase diagram of Fig. 3(c), plotted in (a) using the condensate density ρ . (b) Brillouin zone of the honeycomb lattice (solid) and the triangular lattice obtained by filling the hexagon “voids” (dashed). High-symmetry points and the path used to plot the spectra are indicated. The outer hexagon coincides with the triangular Brillouin zone used in Figs. 4, S5, S6. (c) Magnetic susceptibility obtained by applying LFWT to the full s - \mathbf{T} model. The individual components are shown in red (xx), green (yy), and blue (zz) with the line thickness indicating the intensity. (d) zz component of the magnetic susceptibility obtained using the projected s - T_z model (49) which is equivalent to the pseudospin- $\frac{1}{2}$ model (31) (TFIM extended by $J_{x,y}$ interactions) with the parameters given by Eq. (50). The remaining xx and yy component are zero due to vanishing in-plane g -factors.

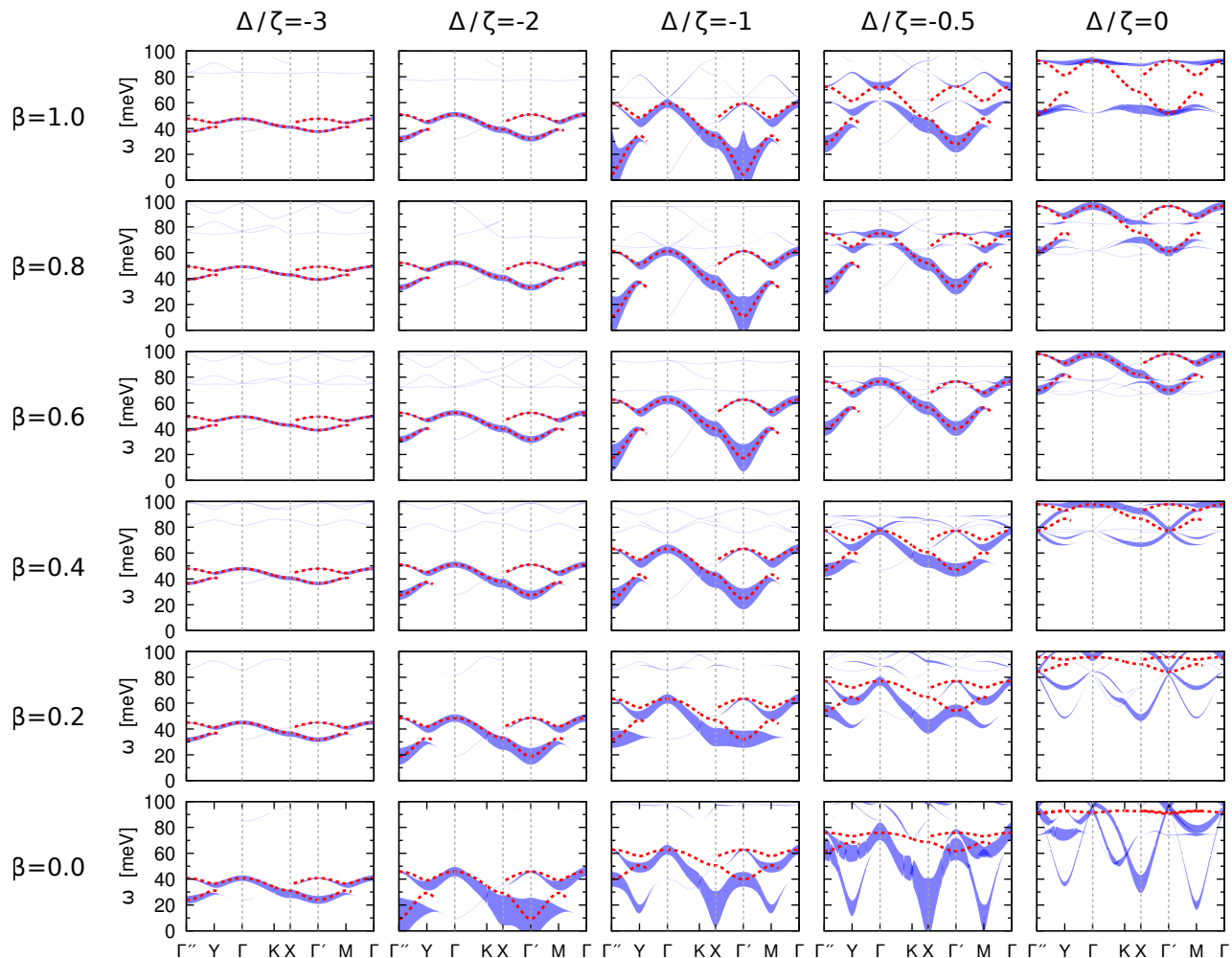


FIG. S4. Comparison of the zz component of the magnetic susceptibility obtained by LFWT applied either to the full $s\text{-}\mathbf{T}$ model (blue) or to the projected $s\text{-}T_z$ model (red dashed). In the former case, the line thickness indicates the intensity as before. In the latter case, to give a hint concerning the intensity, we plot only parts of the dispersion of the corresponding modes where the intensity exceeds certain threshold. The combinations of Δ/ζ and β values cover most of the phase diagram in Fig. S3(a) to give an overall picture.

$s\text{-}\mathbf{T}$ and $s\text{-}T_z$ models, respectively, do not *exactly* coincide in the entire PM phase. As it turns out by an inspection of the interactions within $s\text{-}\mathbf{T}$ model, there is a bilinear coupling between T_z and $T_{x,y}$ bosons for 90° bond geometry which causes the difference observed on the level of LFWT. This coupling becomes negligible around $\beta \approx 0.6$ for our parameter setup, leading to a separation of the modes and the very good agreement observed even at $\Delta/\zeta = 0$, well outside the region governed by pseudospin- $\frac{1}{2}$ model. Far away from $\beta \approx 0.6$, the difference quite significant in our plots for $\Delta/\zeta \geq -0.5$. In the case of the square lattice, such bilinear terms are absent, explaining the perfect match. While for β around 0.6 the pseudospin- $\frac{1}{2}$ model can be pushed surprisingly far beyond its formal range of applicability, in the vicinity of $\beta = 0$ and $\beta = 1$ this extension is further prevented by two complementary kinds of frustration related to a competition among the three T flavors, all being equally active for $\Delta = 0$. Near $\beta = 1$ and $\Delta = 0$, the corresponding singlet-triplet model features Kitaev-like frustration leading to a peculiar ground state with strong but nearest-neighbor only correlations [28]. This is also reflected in the corresponding excitation spectrum in Fig. S4. For $\beta = 0$ and $\Delta = 0$ and neglected Hund's coupling, Ref. [25] found the motion of the triplets of a given flavor to be restricted to a set of parallel zigzag chains on the honeycomb lattice, leading to enhanced quasi-1D behavior. With the Hund's coupling included, the picture changes somewhat, but the treatment based on the trial state (51) still shows a tendency to support non-trivial condensate with a 4-sublattice stripy structure. Such a phase is found in a very narrow region in the phase diagram of Fig. S3(a) ($\beta \lesssim 0.03$ at $\Delta/\zeta = 0$; $\Delta/\zeta \gtrsim -0.6$ at $\beta = 0$). The inspection of the corresponding excitation spectra reveals the characteristic momenta M , Y , X as relevant to this type of condensation.

Triangular lattice

Figures S5 and S6 illustrate the evolution of the magnetic excitations when entering the two condensed phases encountered in the case of the triangular lattice. The corresponding phase diagram is shown in Fig. 3(d) of the main text. The spectra in Fig. S5 are relevant to the clock phase and were discussed in the context of Fig. 4 of the main text. As Fig. S5 demonstrates, the evolution of the dominant out-of-plane component of the magnetic susceptibility is again well reproduced – in the entire range – within the reduced pseudospin- $\frac{1}{2}$ model. However, in the case of Fig. S6 covering the transition into the stripe phase, the pseudospin- $\frac{1}{2}$ model comes out as insufficient due to the significant interaction between the T_z and $T_{x,y}$ bosons which makes the latter ones to participate in the condensation.

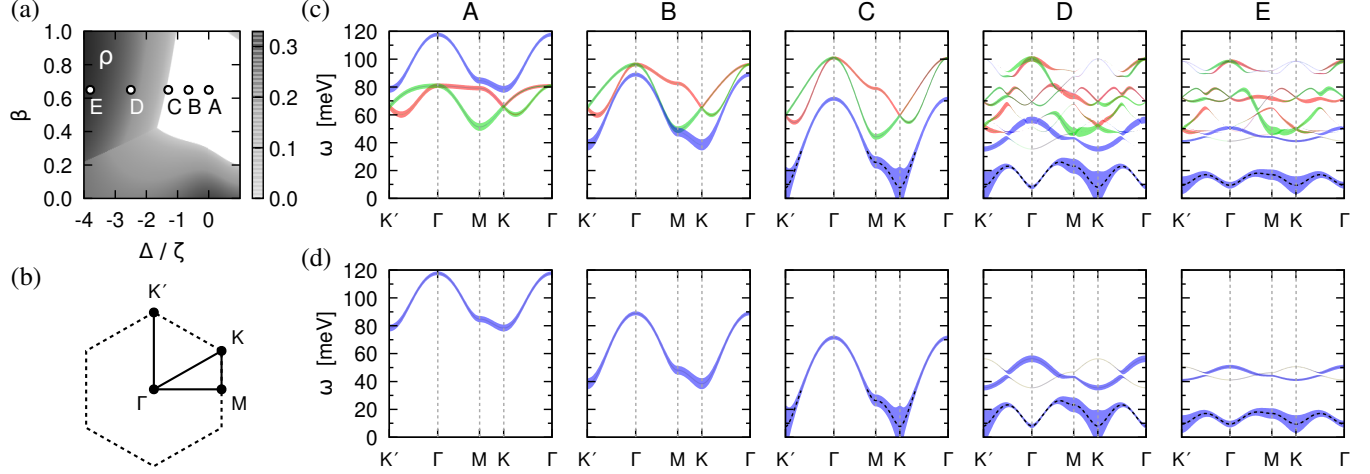


FIG. S5. The same as in Fig. S3 for the triangular lattice and a set of points illustrating the transition from the disordered phase to the clock phase. Again the reduced pseudospin- $\frac{1}{2}$ model in the hardcore boson formulation of Eq. (49) perfectly reproduces the major part of the magnetic excitation spectra.

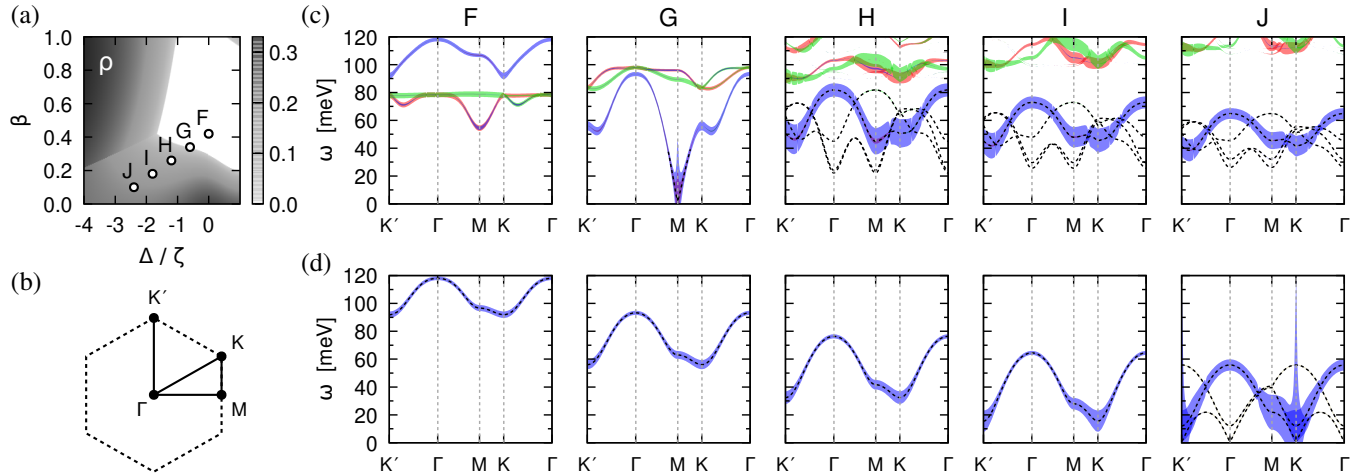


FIG. S6. The same as in Fig. S3 for the triangular lattice and a set of points illustrating the transition from the disordered phase to the stripe phase. Here the reduced pseudospin- $\frac{1}{2}$ model is insufficient since the condensation into stripe phase involves T_x levels in addition to the T_z ones. Therefore the corresponding phase boundary is not detected in (d) and only later (near point J) a transition to the clock phase takes place. However, the full s - T model continues to support the stripe phase in that parameter regime.